Nanoscale

PAPER

View Article Online
View Journal | View Issue

Cite this: *Nanoscale*, 2021, **13**, 20564

One stone two birds: a sinter-resistant TiO_2 nanofiber-based unbroken mat enables PM capture and *in situ* elimination†

Wanlin Xu, ‡[a] Wanlin Fu, ‡[a] Xiangyu Meng, ‡[a] Mingyu Tang,[a] Chaobo Huang,[b] Yueming Sun[a] and Yunqian Dai *[a]

Airborne particulate matter (PM) primarily resulting from fossil fuel burning is an increasingly global issue. In this work, an intrinsically fragile TiO_2 nanofibrous mat was facilely engineered with good structural integrity, flexibility, foldability, and high-temperature resistance (~1300 °C), by suppressing the sintering (*i.e.*, growth) of nanocrystallites in each single nanofiber. Such functionalization enables self-regenerative air filtration for PM capture and *in situ* catalytic elimination in a "one-stone-two-birds" approach. Finite element analysis simulation revealed the retained nanopores in each anti-sintering nanofiber could facilitate the air flow during filtration. Without any chemical or physical modification, this self-standing and lightweight (7.1 g m^{-2}) fibrous mat showed 96.05% filtration efficiency for 3–5 μm NaCl particles, with a low pressure drop of only 18 Pa and high quality factor of 0.179 Pa^{-1} under an airflow velocity of 32 L min^{-1}. By utilizing its photocatalytic attribute, the nanofibrous mat *in situ* eliminated the captured particles from incense burning under one Sun irradiation in 4 h, and thereby spontaneously regenerated in an easy manner. The straightforward grafting of Au nanoparticles onto nanofibers could enable a quick degradation toward cigarette smoke, mainly due to the photothermally elevated local temperature by Au around the reactive sites. The plasmonic fibrous mat kept a high and stable filtration efficiency of $PM_{0.3}$, $PM_{2.5}$, and PM_{10} over 98.62%, 99.76%, and 99.99% during an outdoor long-term filtration test for 12 h under sunlight irradiation (Nanjing, China, September, 26th, 2020, 7:30 to 19:30). This work provides a solution for solving the airborne pollution from its source, prolonging the lifetime of the filter, and avoiding the risk of producing secondary pollution.

Received 6th October 2021,
Accepted 21st November 2021

DOI: 10.1039/d1nr06582c

rsc.li/nanoscale

1. Introduction

Air pollution (*e.g.*, particulate matter (PM), a mixture of small particles in liquid or solid forms) severely threatens human health and the environment, causing 4.2 million deaths annually according to the World Health Organization (WHO).[1,2] There is no doubt that controlling polluted-gas emissions from fossil fuels into the air, without additional energy-consumption, is essential for constructing a clean and energy-efficient low-carbon earth.[3,4] Nowadays, electrospun nanofiber-based mats, a new form of a membrane, are a fresh area of significant focus for air filtration due to their large surface-to-volume ratio, high porosity, and micrometer-sized interstitial space.[5–8] Although many efforts have been made towards ingeniously designing nanofibrous mats based on polymer or carbon with high removal efficiency, it is still challenging to effectively eliminate the airborne particle pollutants, involving strong corrosive conditions and/or high-temperature.[9–12] Considering the inherently good chemical and thermal stabilities, oxide nanofibrous mats hold great promise to capture PM pollutants under harsh conditions without safety issues (*e.g.*, dust explosion, fire). Since the first report of TiO_2 nanofibers in 2003,[13] more than one hundred different types of oxides have been prepared as nanofibers, based on the combination of electrospinning nanotechnology and sol–gel chemistry. By carefully choosing the precursor and tailoring the calcination conditions, the fine structure and the hierarchical architecture (*e.g.*, in-fiber porosity, alignment, and pattern) of nanofibers can be facilely and precisely engineered.[5] However, the daunting challenge of their uses lies in the inherent brittleness of oxide nanofibers. During the necessarily involved calcination process, the tiny nanocrystal-

[a]*School of Chemistry and Chemical Engineering, Southeast University, Nanjing, Jiangsu 211189, P. R. China. E-mail: daiy@seu.edu.cn*
[b]*Jiangsu Key Lab of Biomass-based Green Fuels and Chemicals, College of Chemical Engineering, Nanjing Forestry University, Nanjing, Jiangsu 210037, P. R. China*
†Electronic supplementary information (ESI) available. See DOI: 10.1039/d1nr06582c
‡These three authors contributed equally to this work.

lites in each oxide nanofiber tend to sinter into large particles, thereby leading to densification of the whole nanofiber in an uncontrollable manner. This phenomenon commonly causes the breakage of oxide nanofibers along the grain boundary and loss of structural integrity (easy breaking of the fibers). Upon handling, stress-induced cracks often occur at the grain boundary in the densified, ultralong, and thin nanofiber. As such, small fragments are usually formed rather than free-standing mats. Despite recent success in improving the strength or flexibility by physical and/or chemical modifications,[5,14–16] the brittleness-induced poor structural integrity of oxide fibrous mats still seriously hampers their practical use.

Traditional air filtration materials today still need frequent replacement, causing high labor and cost. This intractable issue is caused by the unfavorable coverage of the capture sites on the surface after long-time filtration. To regenerate the filter, physical approaches, including air blowing and solvent washing, are most commonly utilized.[17,18] However, the problem of second-hand pollution is still concerning, and the fine non-soluble organic particles are in fact not removed.[3] To this end, recent research studies have determined to involve chemical protocols to *in situ* degrade PM pollutants for solving the pollution at its source and extending the filter lifetime. Generally, the as-captured hydrocarbon pollutants can be completely decomposed at a high critical temperature above 550 °C with the aid of a thermal catalyst.[2,19] Involving high-temperature treatment could cause inevitable damage to the polluted filters. Alternatively, UV-light-driven degradation shows the potential of eliminating the airborne fine PM moderately.[20] If endowed with activity and sufficient active sites, solar-driven photocatalytic oxidation can facilely degrade various pollutants into non-toxic form(s) by abundant sunlight under ambient conditions. Furthermore, localizing plasmonic nanoantennas as hot-spots around the captured PM is a new and potential strategy for boosting photocatalytic degradation kinetics to match the rapid pollutant influx and simultaneously enabling the self-regeneration of the air filter. Despite distinctive advantages, coupling plasmonic nanostructures in fibrous mats is still at an early stage for PM degradation. More in-depth studies are required to elucidate the synergistic mechanisms and address such practical issues.

In this work, we demonstrate that an intrinsically fragile TiO_2 nanofibrous mat could be simply functionalized with good structural integrity and foldability, by depressing the growth of nanocrystallites in a single nanofiber. With excellent sinter-resistance, this unbroken mat was explored as a self-regenerative membrane for PM capture and *in situ* catalytic elimination in a "one-stone-two-birds" manner. This self-standing and lightweight (7.1 g m^{-2}) fibrous mat showed 96.05% filtration efficiency for 3–5 μm NaCl particles at room temperature, with a low pressure drop of only 18 Pa and a high quality factor (QF) of 0.179 Pa^{-1} under an airflow velocity of 32 L min^{-1}. When exposed to high-temperature incense particles, the thermally stable mat achieved a high trapping efficiency and was further endowed with photocatalytic degradation capability toward organic pollutants. After decorating plasmonic Au nanoparticles as antennas in an ultralow loading, the plasmonic coupling effect and the localized thermal field boosted the contaminant elimination efficiency. Based on these merits, the catalytic nanofibrous mats showed excellent PM filtration efficiency (99.99%) and durability (12 h) during an outdoor test in Nanjing.

Yunqian Dai

Yunqian Dai was born in Longchang, Sichuan. She received her Ph.D. from Southeast University in 2011 with Prof. Yueming Sun. She spent two years in Prof. Xia's group as a visiting graduate student from 2008 to 2010. She has been a full professor at Southeast University in the School of Chemistry and Chemical Engineering since 2019. Her current research interests include electrospun nanofibers and their applications in catalysis, environmental science, and energy technology.

2. Experimental section

Chemicals

Polyvinylpyrrolidone (PVP, $M_w \approx 1.3 \times 10^6$), titanium isopropoxide (TTIP), and aluminum acetylacetonate ($Al(acac)_3$) were obtained from Alfa Aesar. Gold(III) chloride trihydrate ($HAuCl_4 \cdot 3H_2O$, 99.9%) was purchased from Sigma Aldrich. Sodium borohydride ($NaBH_4$, 98%) was obtained from Macklin. All other chemicals were obtained from Sinopharm Chemical Reagent Co., Ltd. All chemicals were used as received.

Fabrication of TiO_2 and modified-TiO_2 nanofibrous mats

The traditional TiO_2 nanofibrous mat was prepared by electrospinning a precursor containing 0.3 g of PVP ($M_w \approx 1.3 \times 10^6$), 4.5 mL of ethanol, 2.5 mL of TTIP, and 3 mL of acetic acid, with a flow rate of 0.3 mL h^{-1} at 17 kV, followed by calcination at 600 °C for 2 h with a ramping rate of 2 °C min^{-1}, whereas the modified-TiO_2 (noted as *m*-TiO_2) nanofibrous mat was prepared by electrospinning a precursor, which contains 0.6 g of PVP ($M_w \approx 1.3 \times 10^6$), 4.5 mL of ethanol, 1.0 g of $Al(acac)_3$, 5 mL of acetone, 1.4 mL of TTIP, and 3 mL of acetic acid, with a flow rate of 0.5 mL h^{-1} at 18 kV, followed by calcination at 600 °C for 2 h with a ramping rate of 2 °C min^{-1}.

Functionalization of plasmonic Au nanoparticles

The Au nanoparticles were prepared according to a previous report.[21] Specifically, 0.25 mL of 3 g mL^{-1} $HAuCl_4$ solution, 0.25 mL of 0.01 mol L^{-1} sodium citrate solution and 0.25 mL

of ice-cold 0.01 mol L^{-1} $NaBH_4$ solution were added sequentially into 9.25 mL of ultrapure water. Then, the Au nanoparticles were uniformly loaded on the surface of the *m*-TiO_2 mat by electrospraying the Au colloid with a flow rate of 0.3 mL h^{-1}, at 18 kV for 5 min. The obtained filter was denoted as the Au@*m*-TiO_2 mat.

Air-flow simulation in one nanofiber

Simulation results were derived using finite element analysis in COMSOL Multiphysics with the Computational Fluid Dynamics (CFD) Module with a laminar flow interface in the steady-state. The modeling was set based on the measurement from SEM images in Fig. 1. The density was calculated by the weight method. The dynamic viscosity was set as 1 Pa s^{-1}. The initial flow rate at the entrance was set as 0.6 m s^{-1}.

Filtration efficiency evaluation

NaCl mode. The filtration performance toward room-temperature PM particles was evaluated using an LZC-H filter tester (Huada Filter Technology Co., Ltd, China), including the filtration efficiency and pressure drop. During the filtration test, the *m*-TiO_2 mat (effective area of 78.54 cm^2) was clamped by the holder, and then NaCl particles were delivered through the mat steadily and uniformly. All of the air filtration tests were conducted at an ambient temperature of (25 ± 2) °C and humidity of (35 ± 5) % with a controlled flow rate.

Incense and cigarette mode. To measure the filtration efficiency at high temperatures, the PM particles were generated by burning incense or a cigarette in a hermetic room. As shown in Fig. S6,† the filter was placed inside a filter and connected with two chambers. The filtration efficiency (η) can be evaluated using the formula:

$$\eta = \frac{N_t - N_0}{N_0} \times 100\%$$

where N_0 and N_t represent the numbers of PM particles before and after filtration, respectively, recorded using the PM particle counter (XinSiTe HT-9600).

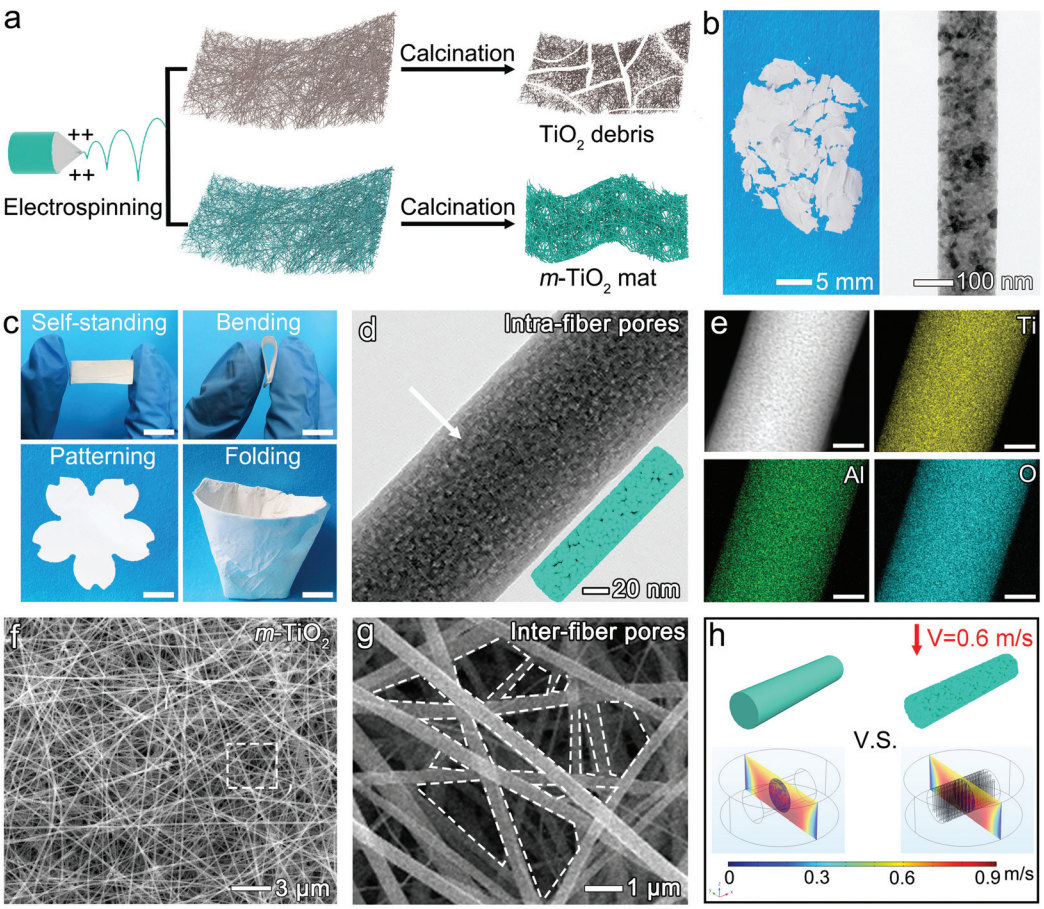

Fig. 1 (a) Schematic fabrication process of TiO_2 debris and the *m*-TiO_2 mat. (b) Optical and TEM images of the traditional TiO_2 nanofiber without modification. (c) Optical images of the *m*-TiO_2 nanofibrous mat with self-supporting nature, flexibility, tailorability, and foldability. The scale bars are 1 cm. (d) TEM image with a schematic illustration of one *m*-TiO_2 nanofiber with tiny nanocrystallites in (c). The white arrow highlighted the intra-fiber pores. (e) HAADF-STEM and the corresponding elemental mapping images of the nanofiber in (d). The scale bars are 20 nm. (f) SEM image of the *m*-TiO_2 nanofibrous mat. (g) The magnified SEM image highlighted in (f) with a white rectangle. The white dotted lines highlighted the opening pores among nanofibers. (h) The simulated air-flow rate on one single nanofiber (left) without and (right) with nanopore structures.

In situ elimination of PM driven by sunlight

After filtration under the incense or cigarette test mode for 5 min, the polluted *m*-TiO_2 mat was taken out and exposed to sunlight irradiation to degrade the pollutants for regeneration. A long-term stability test was carried out in a closed box with a size of 44 cm × 44 cm × 44 cm, as shown in Fig. S13.† The Au@*m*-TiO_2 mat was placed on a circular hole with a diameter of 1 cm above the closed box, and the numbers of PM particles were recorded in 30 min intervals for the calculation of η. The outdoor test was conducted in Nanjing, China, on September, 26th, 2020, from 7:30 to 19:30.

Characterization

Transmission electron microscopy (TEM) images were obtained using a transmission electron microscope (Tecnai G2 T20, FEI) operated at 200 kV. High-resolution transmission electron microscopy (HRTEM) and high angle circular dark-field scanning transmission electron microscopy (HAADF-STEM) images and energy dispersive spectroscopy (EDS) results were obtained using a Talos F200X system. Scanning electron microscopy (SEM) and Energy Dispersive X-ray (EDX) measurements were obtained using an FEI field-emission microscope (Nova Nano SEM 230). The sample for SEM measurement was sputtered with Pt using an ion sputtering instrument (Hitachi, e-1010). The electron spectrum information of the sample was obtained by X-ray photoelectron spectroscopy (AXIS Supra, Kratos). Fourier transform infrared spectroscopy (FTIR) (Nicolet 5700) was used to monitor the chemical bonds changing in fresh, PM captured, and regenerated *m*-TiO_2 mats. The nanofiber diameter and pore area were measured using the Image J software (National Institutes of Health, Bethesda, MD, USA, 2009), available at http://imagej.nih.gov/ij. The Brunauer–Emmett–Teller (BET) specific surface area and Barrett–Joyner–Halenda (BJH) pore size distribution were measured using a Nova 1200e system (Quantachrome, U.S.A.). The sunlight irradiation was operated using a Xe lamp (CEL-HXF300/CEL-HXUV300, CEAULIGHT Co., Beijing, China). The infrared images were taken using a thermal imager (FOTRIC 600C). The content of Au on the nanofiber was measured by the inductively coupled plasma atomic emission spectrometry (ICP-AES, Shimadzu ICP-7510).

3. Results and discussion

Synthesis of unbroken and foldable *m*-TiO_2 nanofibrous mats

As shown in Fig. 1a, the traditional TiO_2 nanofibrous mats can be readily fabricated *via* a facile electrospinning technology combined with calcination. Conventionally, electrospun TiO_2 nanofibers are extremely fragile after calcination, and even difficult to be handled due to the sintering of nanocrystallites (Fig. 1a and b).[14] However, after depressing the sintering of nanocrystallites and restoring nanopores inside TiO_2 nanofibers *via* blending a small amount of Al_2O_3, a self-standing, flexible, and foldable mat was easily obtained (Fig. 1c and d). Inspired by origami technology, an *m*-TiO_2 mat with a small thickness (~30 μm) could be easily folded into a 3D "ceramic cup" with a low volume density of 0.037 g cm^{-3} (Movie S1†). When serving as an air filter (*e.g.*, a cigarette filter), pollutant particles can be efficiently intercepted within such a 3D "ceramic cup" by highly connected nanofibers.[22,23] This new attribute holds great promise in energy and environment-related applications, requiring light-weighted, foldable, and portable features.

The unique flexibility of the *m*-TiO_2 mat was remarkably contributed by the ably design within a single nanofiber at the nanoscale level. As shown in Fig. 1b, the traditional TiO_2 nanofibers consist of fused nanocrystallites with a size of ~36 nm (measured based on the TEM image). Under thermal stress (600 °C), these ceramic nanofibers would suffer from structural collapse along the grain boundary and tend to crack into small pieces. This poor structural integrity greatly hinders their practical applications. After introducing a small amount of Al_2O_3, tiny nanocrystallites with enriched intra-fiber pores formed within each *m*-TiO_2 nanofiber, as highlighted in Fig. 1d. Also notably, the size of nanocrystallites decreased sharply to ~13.7 nm (calculated based on the XRD result), which may effectively improve the mechanical strength of the resultant *m*-TiO_2 nanofibers. According to the well-known Hall–Petch effects, nanomaterials with smaller sizes exhibit significantly enhanced mechanical strength, due to their increased interfacial areas in the form of grain boundaries.[14] Moreover, the XRD patterns further indicated the crystal structure of the *m*-TiO_2 nanofibers. As shown in Fig. S1,† the characteristic peaks at 25.16° and 48.07° correspond to the (101) and (200) planes of anatase (JCPDS 21-1272).[24] No characteristic peak could be assigned to crystalline Al_2O_3 or rutile-TiO_2. The EDS mappings of Ti, Al, and O shown in Fig. 1e also confirmed the uniform distribution of Al_2O_3 in the whole nanofiber. The lattice parameters of anatase nanocrystallites in the Al_2O_3-modified TiO_2 nanofiber can be calculated to be 0.367 nm, which is smaller than that of a pure TiO_2 nanofiber (0.379 nm). This can be possibly ascribed to the introduction of Al^{3+} into the anatase-TiO_2 lattice since the radius of Al^{3+} (0.054 nm) is smaller than that of Ti^{4+} (0.061 nm).[25,26] In this case, the sintering of TiO_2 nanocrystallites was highly hampered, maintaining a small crystal size and anatase phase after calcination at 600 °C.

As shown in Fig. S2,† inter-fiber pores naturally formed among the interconnected nanofibers during electrospinning. The intra-fiber pores with a BJH pore size of 2.56 nm and a pore volume of 0.057 cm^3 g^{-1} were generated by selective removal of the polymer matrix (*i.e.*, PVP) within the nanofibers during calcination at 600 °C (Fig. 1f and g). The average equivalent diameter of the inter-fiber pore slightly decreased from 0.74 μm to 0.58 μm, owing to the restricted grain growth and small shrinkage of the nanofiber diameter during sintering under calcination. These unique pore structures restored within each nanofiber may buffer the stress induced by high-flux air and the practical handling, thus ably maintaining the structural integrity well. Besides, the nanopore structure in a

single nanofiber also has a special impact on lowering the pressure drop, as further investigated by simulation in Fig. 1h. The model and the setting of fluid are shown in Fig. S4† in detail. It could be seen that the nanopores could offer abundant pathways of airflow, allowing gas to pass through at a high velocity, thus greatly reducing airflow resistance compared to the densified, non-porous nanofibers.[27] These numerous nanopore structures enabled a high surface area of the *m*-TiO_2 nanofibers up to 78.8 $m^2\ g^{-1}$ (Fig. S5†). This surface area is ~180-times superior to that of the commercial high-efficiency particulate air (HEPA) filter standards, and 3.8-times higher than recently reported aerogel filters.[3] Therefore, this unbroken, foldable *m*-TiO_2 mat with hierarchical pore structures (inter-fiber and intra-fiber) is expected to become an advanced air filter to capture the high-throughput PM airflow stably and efficiently.

Filtration capacity and durability of *m*-TiO_2 mats

Nowadays, exhaust gases produced under industrial conditions, such as metallurgy and electric power generation, have become the most destructive culprit, because of their extremely high temperature and complex components, including CO_x, NO_x, SO_x, and some toxic substances.[16] In this case, the design of a new filter with chemical stability, thermal stability, and high-throughput gas treatment is crucial to solving air pollution. As shown in Fig. 2a, the *m*-TiO_2 mats maintained good structural integrity after soaking in strong acid (pH = 2, HCl solution) and strong alkali (pH = 12, NaOH solution) for 30 min, and drying in an oven at 80 °C, showing excellent chemical stability. Moreover, we were surprised to observe that the nonflammable *m*-TiO_2 mat could maintain its original shape and good structural integrity after being combusted by an alcohol lamp (Movie S2†) and a butane blowtorch at ~1300 °C for 60 s (Fig. 2b, Movie S3†). No mat breaking appeared. The SEM investigations further demonstrated the nanostructural evolutions of nanofibers, where the nanocrystallites grew slightly without breaking at the grain boundary (Fig. 2c). However, the pristine as-spun composite nanofibers suffered from much more severe sintering upon calcination at ~1300 °C for 60 s, showing a densified bamboo-like structure (Fig. 2d). The long and thin nanofibers cracked along two sintered grains and broke into short segments. This is easy to understand because the releasing rate and amount of the gaseous substances produced by the decomposition are out of control, causing inhomogeneity of the resultant oxide nanocrystallites and the microscopic pores. In this case, the chemical potential of the nanocrystallites was unevenly distributed across the whole nanofiber, thereby offering a strong driving force toward sintering into larger particles.[28] In sharp contrast, the well-controlled grains in the pre-calcined *m*-TiO_2 nanofiber enable it to sustain high temperatures against sintering successfully.

When the burnt incense passed through the nanofibrous mat (~40 μm of thickness) from the left to right chamber (Fig. S6†), the PM was effectively captured in large quantities (Fig. 2e). There were no cracks observed on the flexible porous mat even after the filtration of high-temperature burnt incense (Fig. 2h and i). More interestingly, the gas temperature dropped almost 30 °C after passing the *m*-TiO_2 mat (Fig. 2f). Taking the thermal catalytic activity of the oxide into consideration, it is reasonable to speculate that waste heat could catalytically drive the thermal degradation of the captured organic matter to a certain extent.[3] As summarized in Fig. 2g, the filtration efficiencies of the *m*-TiO_2 mats toward $PM_{0.3}$, $PM_{2.5}$, and PM_{10} were determined to be 99.18, 99.84, and 99.57%, respectively. As a comparison, commercial melt-blowing polypropylene mats were applied in such a burnt incense filtration setup. Filter-1 (Fig. 2h-ii) is collected from a disposable medical mask (Xiantao Dingcheng non-woven products Co. Ltd) with a thickness of ~86 μm, while filter-2 (Fig. 2h-iii) is collected from an activated carbon procedure earloop mask (Vitals, A.R. Medicom Inc. (Asia) Ltd) with a thickness of ~135 μm. As shown, these commercial filters were seriously damaged and even were inflamed by the high-temperature exhaust gas within 2 min, showing that the filtration efficiencies dropped to almost 0.

To investigate the filtration capacity of the *m*-TiO_2 mat and make a better comparison with previous reports, the filtration test of NaCl particles was also conducted at room temperature. As shown in Fig. 2i, with an increase of airflow velocity, the filtration efficiencies decreased slightly, but were all over 90%, associated with the corresponding low-pressure drop values of 18.0, 68.5, and 89.3 Pa. Generally, an ideal filter should possess a high filtration efficiency and a low-pressure drop to maximize the quality factor (QF), which is defined as $-\ln[(1-\eta)]/\Delta p$, where η and Δp represent the filtration efficiency and pressure to push the air through, respectively.[10] The higher the QF value is, the better the performance will be for filtration. The corresponding QF values of the *m*-TiO_2 mat at flow rates of 32, 64, and 85 L min^{-1} were determined to be 0.179, 0.042, and 0.027 Pa^{-1}, respectively. As summarized in Fig. 2j, the *m*-TiO_2 mat demonstrated prominent filtering capability.[9–12,27,29–33] Notably, the *m*-TiO_2 air filter with high filtration performance also features light weight (an areal density of 7.1 g m^{-2}, only 2.8-times that of a silk filter[34]), which is much lower than the commercial air filters (such as KN90 with 203 g m^{-2}).

Generally, the airborne PM is a chemical mixture of small solid particles and liquid droplets suspended in air, consisting of various chemical components that include both inorganic (*e.g.*, silicates, sulfates, and nitrates) and organic (organic compounds and elemental carbon) matter, which are mainly hydrophilic.[35] The contact angle test in Fig. S7† indicated good affinity of the surface of our *m*-TiO_2 mat to hydroxyl/water, with a water contact angle (WCA) of 14.9° and an underwater oil contact angle (UOCA) of 156.2°. Therefore, the high-polarity hydrophilic *m*-TiO_2 nanofibers offer strong bonding for PM and efficiently trap it on their surface.[36] The capture mechanism of airborne PM by a fibrous mat is mainly based on the following processes: Brownian diffusion, direct interception, inertial impaction, gravity, and chemical/physical or electrostatic attraction.[30] Specifically, the capture of PM on the *m*-TiO_2 air filter was a dynamic process, hypothetically through

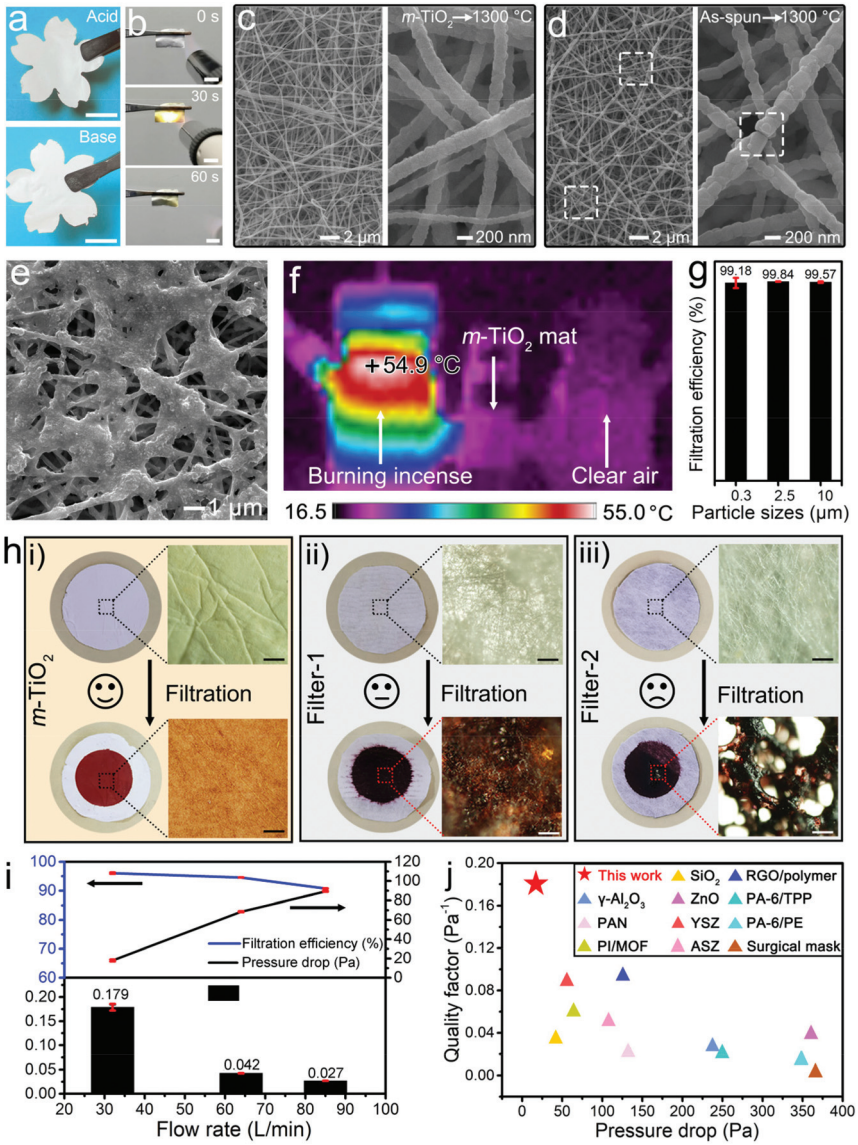

Fig. 2 The optical photos of fibrous mats, showing the (a) chemical and (b) thermal stability. The scale bars are 1 cm. SEM images of (c) *m*-TiO_2 and (d) pristine as-spun composite mats after being heated to ~1300 °C for 60 s using a butane blowtorch, respectively. The white rectangle in (d) highlights the broken nanofibers. (e) SEM image of the *m*-TiO_2 mat after capturing PM from burning incense. (f) The infrared image of an incense burning filtration setup. (g) The filtration efficiency of PM from the burning incense by an *m*-TiO_2 mat. (h) A comparison of the optical images and optical microscopy images of (i) the *m*-TiO_2 mat and (ii and iii) the commercial masks before and after filtration. The scale bars are 5 mm. (i) Filtration efficiency, pressure drop, and quality factor of the *m*-TiO_2 mat at different flow rates of the NaCl aerosol. (j) Comparison of the filtration performance of different recent filtration materials, showing the unique merits of our mat.

the following three steps. (i) At the beginning, low amounts of PM were captured by the mat and then located randomly on the *m*-TiO_2 nanofibers. (ii) With the accumulation of PM, adjacent liquid aerogels gradually merged into larger droplets, and solid aerogels formed dendritic structures on the fibrous surface. In this case, the pressure drop increased significantly. Recent research has studied the dynamic process of PM capture. For liquid form in PM, the wetted droplets tend to aggregate into axisymmetric structures, while non-wetted droplets aggregate into non-axisymmetric structures.[37] (iii) Eventually, with further accumulation, the opening pores and channels within the *m*-TiO_2 mat would be completely blocked. In this case, the pressure drop reaches the maximum and the filter fails. Although some studies have reported that the service life of the filter can be effectively prolonged through technologies such as reverse purification and washing, the residual non-soluble organic particles and the second-hand pollution of the removed PM are still intractable.

Self-regenerative air filter driven by sunlight

TiO_2 exhibits appreciable photocatalytic activity for degrading pollutants into non-toxic or less harmful forms, including the

degradation of dyes from aqueous solution,[38] solid polystyrene particles,[39] and gaseous VOCs.[40] In a typical photocatalytic degradation process, the electron–hole pair generated upon the interaction of TiO_2 with UV-light further interacts with adsorbed oxygen, water, and hydroxyl groups (–OH) to produce various active species which are transferred into contaminants leading to radical initiated photodegradation reactions. However, the degradation of PM is still a great challenge because the complex compositions of PM (mixture of liquid and solid forms) make the triggering of the photocatalytic reaction in a sluggish manner. The loose contact between the captured PM and TiO_2 further seriously hinders the reaction at solid/solid and liquid/solid interfaces.[41] Also, the inherent wide bandgap and the rapid recombination of charge carriers in bulk TiO_2 lead to a narrow solar spectrum response region and low quantum efficiency.[25] In our demonstration, the captured PM on the *m*-TiO_2 mat was gradually degraded under sunlight irradiation (one Sun) in a short period of 4 h (Fig. 3a–c). The degradation reaction was initiated at the interface between the captured PM and the clean TiO_2 with exposed sites. As the light-irradiation time prolonged, more available active TiO_2 sites were exposed and enabled the photodegradation rate to increase in an accelerating manner. By prolonging the illumination time, the captured PM on the nanofibers was entirely removed.

To further explore the revolution of the captured substances on the *m*-TiO_2 mat under sunlight, FTIR was employed to monitor the chemical bonds changing in fresh, PM captured, and regenerated mats. As observed in Fig. 3d, there were three new peaks emerging at 1247, 1405, and 1573 cm^{-1} after filtering burning-incense smoke, which are assigned to aromatics, alcohols, and amides, respectively.[42] After irradiation, these three characteristic peaks decreased greatly, verifying the degradation of organic components in PM pollutants.

The composition and surface chemistry of *m*-TiO_2 mats before and after sunlight-driven regeneration were also investigated by XPS characterization. The XPS survey spectrum of the adsorbed-*m*-TiO_2 mat in Fig. 3e also showed that the main

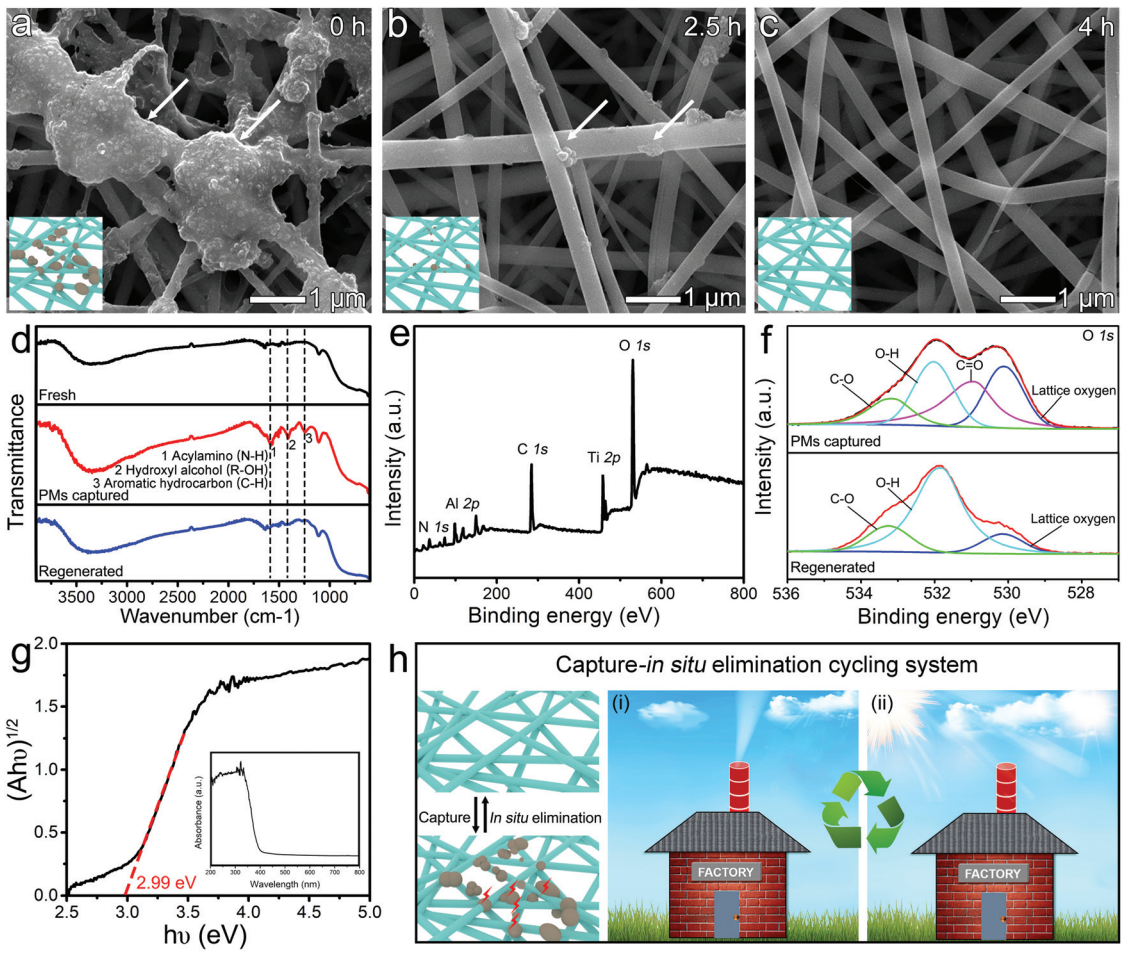

Fig. 3 SEM images of burning-incense particles on *m*-TiO_2 mats under sunlight irradiation for (a) 0, (b) 2.5, and (c) 4 h. The insets are schematic diagrams of the regenerated nanofibrous mats. (d) FTIR spectra of fresh, PM-captured and regenerated *m*-TiO_2 mats. (e) XPS survey of the *m*-TiO_2 mat after filtration. (f) O 1s XPS spectra of the PM-captured and regenerated *m*-TiO_2 mats by sunlight irradiation. (g) Tauc plot of the *m*-TiO_2 nanofibers. The inset shows the corresponding UV–vis spectrum. (h) Schematic diagram of capture-*in situ* elimination behavior enabled by the *m*-TiO_2 mat in the purification of the pollutant gas exhausted from a modern factory.

elements were Ti, Al, O, C, and N. As shown in Fig. 2e and Fig. S8,† the coverage of the captured PM on the mat remarkably decreased from 85.1% to 1.5% after the photocatalytic degradation. Besides, as depicted in Fig. 3f, the O 1s XPS spectrum of the PM captured *m*-TiO_2 mat can be well modelled by four components, ascribed to the lattice oxygen (530.10 eV), C═O bond (530.90 eV), C–OH bond (532.03 eV) and C–O (533.13 eV), respectively.[43] After the photocatalytic degradation, the typical characteristic peak of C═O disappeared, indicating the removal of the organic species in the PM pollutants. Besides, the bandgap energy of the *m*-TiO_2 mat was reduced to 2.99 eV (less than the reported anatase with 3.2 eV, and the rutile with 3.0 eV),[25] after being blended with Al_2O_3 in a small content. Therefore, the narrowed bandgap and the clean surface could lead to the efficient broadening of the light absorption range and were beneficial to drive the oxidative decomposition of PM pollutants under sunlight.

By combining the filtration with the photocatalytic process, the *m*-TiO_2 mat holds great promise in constructing a capture-*in situ* elimination cycling system by dynamically removing the captured PM on the fibrous mat under sunlight. As shown in Fig. 3h, in the filtration process, high-flux PM particles are efficiently intercepted on the *m*-TiO_2 mat with the help of porous structures. Meanwhile, driven by sunlight, the *m*-TiO_2 mat can effectively degrade pollutants, release catalytic sites covered by the adsorbent, and thus achieve self-regeneration.

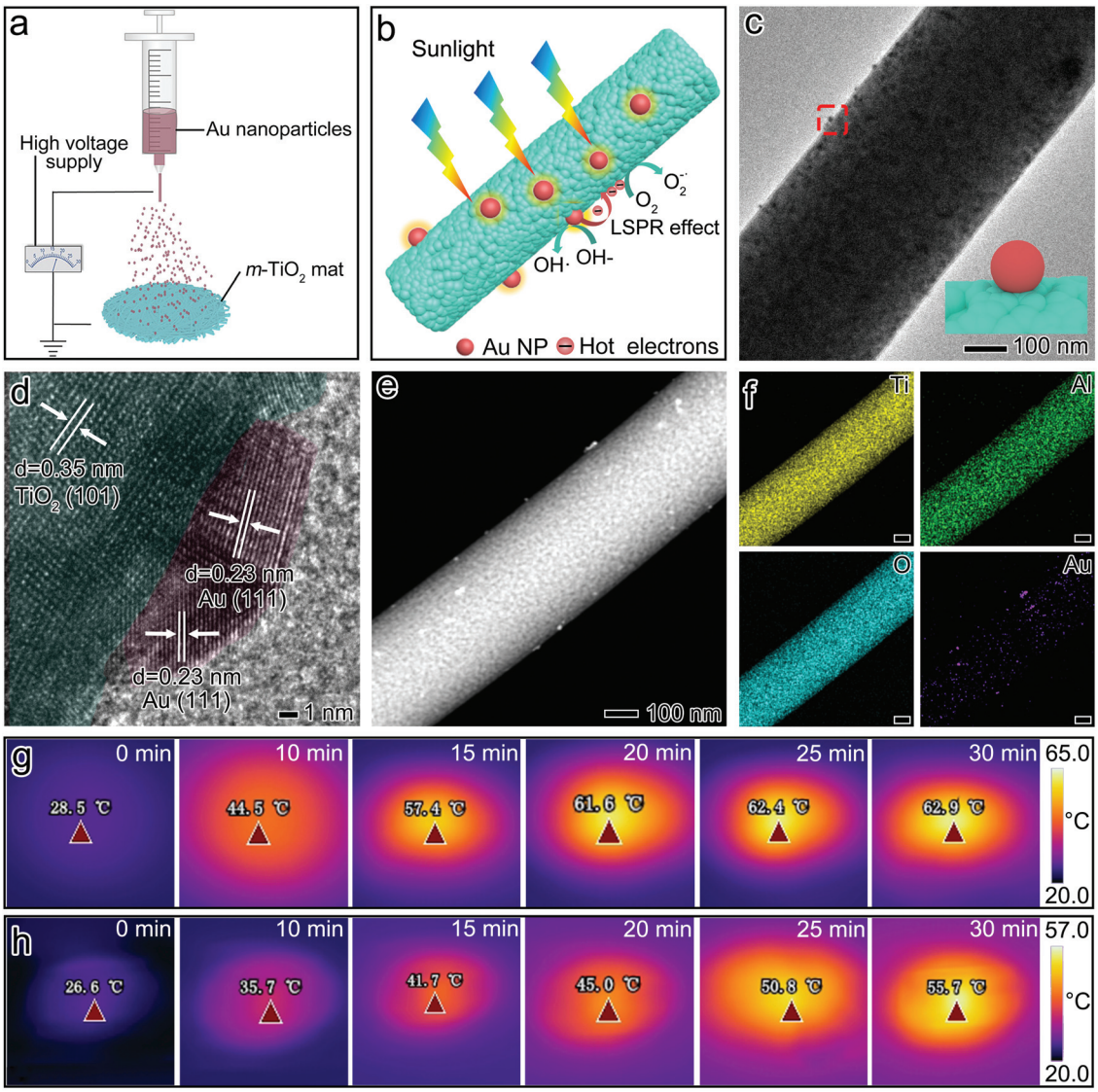

Fig. 4 (a) Schematic illustration of the decoration of Au nanoparticles on the *m*-TiO_2 nanofibrous mat by electrospraying. (b) Schematic diagram of the photocatalytic mechanism of the Au@*m*-TiO_2 mat in sunlight. (c) TEM image of the Au@*m*-TiO_2 nanofiber with the schematic illustration of the interface between the Au and *m*-TiO_2 nanofibers. (d) HRTEM, (e) HAADF-STEM, and (f) elemental mapping images of Ti, Al, O, and Au in one representative Au@*m*-TiO_2 nanofiber. The scale bars in (f) are 10 nm. The infrared images of (g) Au@*m*-TiO_2 and (h) *m*-TiO_2 mats under one Sun irradiation.

Usually, the slow photocatalytic degradation rate of PM is disabled to match the rapid influx of PM onto fibrous surfaces in real-time, which calls for reliable methods for accelerating the photocatalytic cleaning process.

Localized plasmonic nanostructure for boosting the self-regeneration of the air filter

For boosting the photocatalytic regeneration of the fibrous mat, plasmonic Au nanoparticles were uniformly anchored on the *m*-TiO_2 nanofibers (denoted as Au@*m*-TiO_2) by facile electrospraying (Fig. 4a). As schematically illustrated in Fig. 4b, these plasmonic Au anchored on a fibrous mat are expected to accelerate the air-pollutant degradation by plasmonic photocatalysis. First, the UV–vis spectra of the Au@*m*-TiO_2 mat in Fig. S9† demonstrated the localized surface plasmon resonance (LSPR) peak of Au nanoparticles at around 540 nm. The plasmonic coupling effect between the randomly located Au nanoparticles and the Au–TiO_2 hybrids can effectively broaden the photon absorption range, and thereby further enhance the light-harvesting.[44,45] Second, the photoinduced high-energy hot-electrons in Au could be directly utilized and/or be transferred to come into contact with TiO_2, offering great promise to enhance the activity of pollutant photodegradation. Third, the local thermal field surrounding Au could accurately elevate the local temperature for reducing the activation energy of the reaction and boosting the mass diffusion.[46,47] Notably, this local heating can be ably localized on the active sites for air-pollutant degradation. This approach is more energy-efficient in promoting the reaction kinetics than that recently demonstrated on bulk heating within a thermal-catalyst filter.[3]

The decoration of Au nanoparticles on the *m*-TiO_2 nanofiber was further confirmed by the clear distribution of Ti, Al, O, and Au elements in EDS mapping. The HRTEM images (Fig. 4d and Fig. S10†) showed that the Au nanoparticles came into close contact with the nanofiber, which facilitates the effective transfer of hot-electrons and/or -carriers from Au to TiO_2 sites.[48,49] It is worth noting that the loading ratio of Au was only 0.008 wt% in the whole mat. Such an ultra-low Au loading enables efficient photothermal conversion and local heating. A large temperature increase of 34.4 °C within the whole mat and a high photothermal conversion efficiency of 86% was obtained under one Sun irradiation (superior to its counterpart, Fig. 4g, h and S11†). Under irradiation, the hot electrons that escaped from the plasmonic Au nanostructures can be rapidly injected into the nearby TiO_2, ultimately converting them into heat through relaxation with a high local temperature, and serving as high-energy electrons for participating in the electron transition.[49] These high-energy hot electrons could be trapped in the surface oxygen vacancies with a prolonged lifetime. They could effectively transfer to the

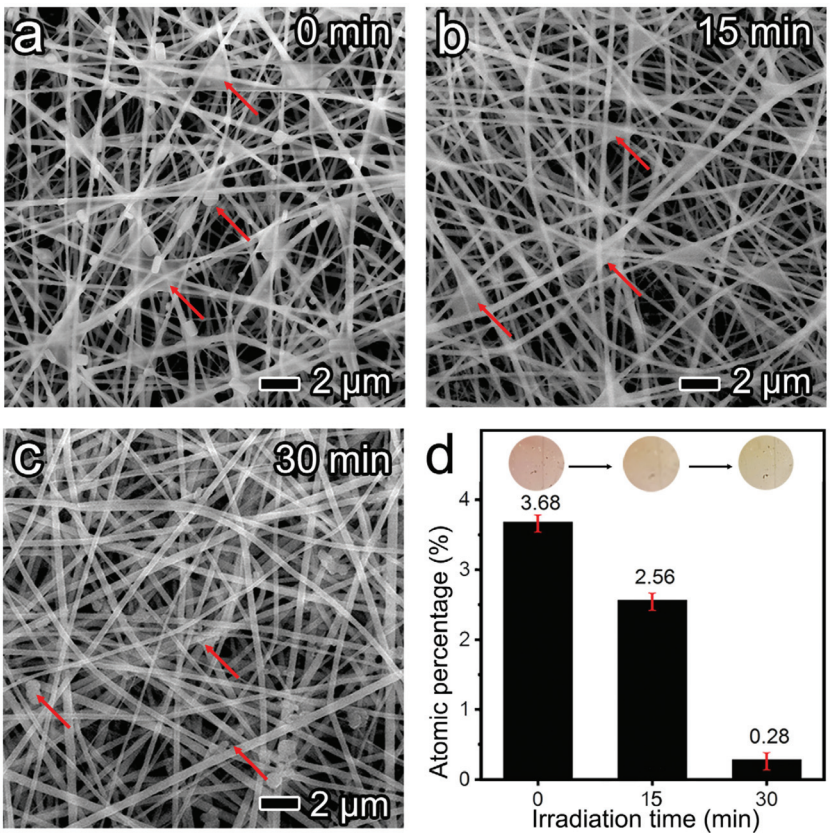

Fig. 5 SEM images of the Au@*m*-TiO_2 mat polluted by cigarette smoke particles (a) before and after 2.2 Sun irradiation for (b) 15 and (c) 30 min. (d) Carbon atomic percentage on the filter *versus* irradiation time. The insets show the corresponding optical photos.

absorbed O_2, producing highly reactive oxygen species (*e.g.*, $^{\bullet}O^{2-}$) for PM oxidation.[50] In this way, the strong local thermal field could heat the reactive sites in an effective manner solely powered by sunlight, boosting the photocatalysis and free-radical attack of PM, even at the loosely contacted solid/solid interface.

If illuminated by an artificial sun with higher light intensity, which is fashionable in industrial factories, regeneration can be achieved in a further accelerated manner. As shown in Fig. 5, the Au@*m*-TiO_2 mat, with only 0.008 wt% of Au nanoparticles, surprisingly degraded the cigarette smoke within 30 min under 2.2 Sun. It should be noted that cigarette smoke contains 92% of gaseous pollutants including carbon monoxide, hydrocyanic acid, and ammonia, and 8% of particulate matter, which is collectively called tar, composed of nicotine, polycyclic aromatic hydroxyl, benzopyrene, β-naphthylamine, *etc.* These contaminants are not only carcinogens but also hard to degrade. The SEM observation indicated that the area of pollutants decreased significantly and eventually disappeared, indicating that there was no blind spot of decomposition. The corresponding EDX results (Fig. 5d and S12†) showed that the carbon-containing contaminants rapidly decreased by 92.4% within 30 min.

Benefitting from the dynamic regeneration and self-cleaning of active sites, the Au@*m*-TiO_2 mat exhibited excellent reusability and long-term stability for the filtration test. As shown in Fig. 6a and S13,† the reusability of the Au@*m*-TiO_2 mat was tested in the "pollution–photodegradation–filtration test" cycle 6 times with continuous burning of incense. After 6 cycling tests, the filtration efficiencies of the Au@*m*-TiO_2 mat for $PM_{0.3}$, $PM_{2.5}$, and PM_{10} were 97.46%, 99.60%, and 99.99%, respectively. Besides, the filtration efficiencies of the Au@*m*-TiO_2 mat for $PM_{0.3}$, $PM_{2.5}$, and PM_{10} were over 98.62%, 99.76%, and 99.99% during the outdoor long-term filtration test for 12 h (Fig. 6b, Nanjing, China, September, 26th, 2020, 7:30 to 19:30). These results showed that the Au@*m*-TiO_2 mat with ably recyclability and stability is a potential alternative material for practical air filtration with unique self-cleaning features. The inset in Fig. 6b shows a promising application scenario of this *m*-TiO_2 mat in the modern factory. We believe that this unbreakable, lightweight *m*-TiO_2 mat can be easily integrated into a current air filtration system. Driven by sunlight, this mat directly degrades captured pollutants in real-time, reducing the blockage of the filtration materials and their replacement in high frequency. Meanwhile, it reduced the risk of second-hand pollution, which is often accompanied by other filter regeneration methods, including wind blowing, washing, or calcination. This self-regenerative filtration system paves the way for overcoming the air pollution that severely endangers human health.

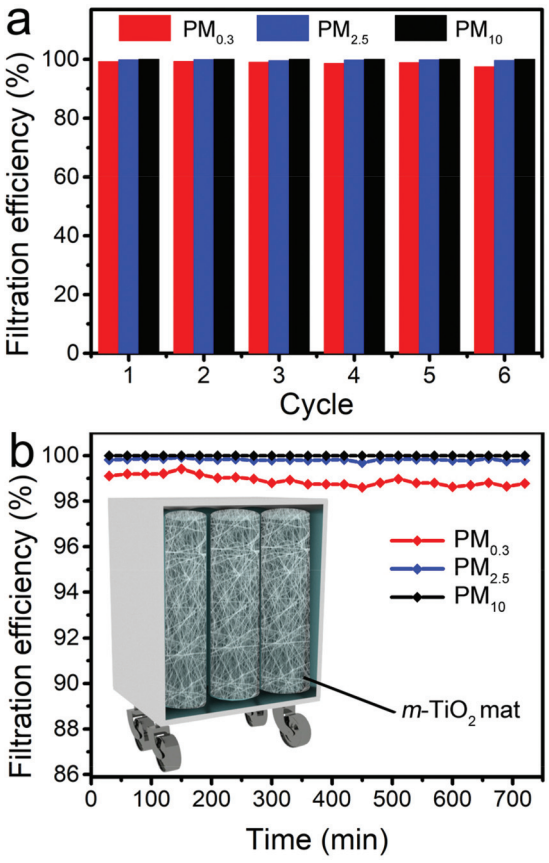

Fig. 6 PM removal efficiencies of the Au@*m*-TiO_2 mat (a) over six cycles and (b) for the outdoor long-term filtration process. The inset in (b) shows the schematic illustration of a portable, high-temperature resistant, recyclable air-purification device integrated with the *m*-TiO_2 mat.

4. Conclusion

In this work, we demonstrated that a traditional fragile fibrous TiO_2 mat could be simply engineered with good structural integrity, flexibility, and foldability by hampering the sintering of nanocrystallites in a single nanofiber with high-temperature endurance ~1300 °C. This unique feature enables the PM capture and *in situ* catalytic elimination in a new "one-stone-two-birds" strategy. Benefiting from the interconnected pores and good air permanence, this self-standing and lightweight fibrous mat showed a high filtration efficiency of over 99.84% for burnt incense, and photocatalytically degraded the captured incense particles in 4 h under one Sun irradiation. After anchoring plasmonic Au nanoparticles on the mat at an ultra-low-content, a strong plasmonic thermal field was ably localized on the reactive sites, with efficient local heating for remarkably boosting the contaminant elimination efficiency. Due to its unique and rapid regeneration features, the Au@*m*-TiO_2 mat maintained a stable filtration efficiency of 99.99% for airborne PM_{10} even after an outdoor long-term test over 12 h. This thermally stable mat is promising for high-temperature exhaust gas filtration with good work safety in metal processing, power generation, or the chemical industry, and could potentially solve PM pollution at its source.

Conflicts of interest

There are no conflicts to declare.

Acknowledgements

This work was financially supported by the National Natural Science Foundation of China (21975042), the Project of Six Talents Climax Foundation of Jiangsu (XCL-082), the Young Talent Lifting Project of Jiangsu Science and Technology Associate, the Fundamental Research Funds for the Central Universities, and the Priority Academic Program Development of Jiangsu Higher Education Institutions.

References

1 J. Zivin and M. Neidell, *Science*, 2018, **359**, 39–40.
2 *Ambient Air Pollution: A Global Assessment of Exposure and Burden of Disease*, Inis Communication, World Health Organization, 2016.
3 X. Ji, J. Zhao, S. Jung, A. Hrdina, M. Wolf, X. Yang, G. Vaartstra, H. Xie, S. Luo, A. Lu, R. Welsch, E. Wang, L. Li and J. Kong, *Nano Lett.*, 2021, **21**, 8160–8165.
4 H. Liu, C. Cao, J. Huang, Z. Chen, G. Chen and Y. Lai, *Nanoscale*, 2020, **12**, 437–453.
5 J. Xue, T. Wu, Y. Dai and Y. Xia, *Chem. Rev.*, 2019, **119**, 5298–5415.
6 W. Zhu, Y. Cheng, C. Wang, N. Pinna and X. Lu, *Nanoscale*, 2021, **13**, 9112–9146.
7 X. Du, Q. Li, G. Wu and S. Chen, *Adv. Mater.*, 2019, **31**, 1903733.
8 L. Shang, Y. Yu, Y. Liu, Z. Chen, T. Kong and Y. Zhao, *ACS Nano*, 2019, **13**, 2749–2772.
9 C. Liu, P. Hsu, H. Lee, M. Ye, G. Zheng, N. Liu, W. Li and Y. Cui, *Nat. Commun.*, 2015, **6**, 6205.
10 H. Wang, S. Lin, S. Yang, X. Yang, J. Song, D. Wang, H. Wang, Z. Liu, B. Li, M. Fang, N. Wang and H. Wu, *Small*, 2018, **14**, 1800258.
11 P. Zhang, D. Wan, Z. Zhang, G. Wang, J. Hu and G. Shao, *Environ. Sci. Nano*, 2018, **5**, 1813–1820.
12 Z. Hao, J. Wu, C. Wang and J. Liu, *ACS Appl. Mater. Interfaces*, 2019, **11**, 11904–11909.
13 D. Li and Y. Xia, *Nano Lett.*, 2003, **3**, 555–560.
14 Y. Zhang, S. Liu, J. Yan, X. Zhang, S. Xia, Y. Zhao, J. Yu and B. Ding, *Adv. Mater.*, 2021, 2105011.
15 H. Shan, X. Dong, X. Cheng, Y. Si, J. Yu and B. Ding, *Nanoscale*, 2019, **11**, 14844–14856.
16 C. Jia, Y. Liu, L. Li, J. Song, H. Wang, Z. Liu, Z. Li, B. Li, M. Fang and H. Wu, *Nano Lett.*, 2020, **20**, 4993–5000.
17 R. Wang, Y. Li, Y. Si, F. Wang, Y. Liu, Y. Ma, J. Yu, X. Yin and B. Ding, *Nanoscale Adv.*, 2019, **1**, 1948–1956.
18 S. Jeong, H. Cho, S. Han, P. Won, H. Lee, S. Hong, J. Yeo, J. Kwon and S. Ko, *Nano Lett.*, 2017, **17**, 4339–4346.
19 Z. Zhu, W. Wang, D. Qi, Y. Luo, Y. Liu, Y. Xu, F. Cui, C. Wang and X. Chen, *Adv. Mater.*, 2018, **30**, 1801870.
20 K. Sohara, K. Yamauchi, X. Sun, K. Misawa and Y. Sekine, *Catalysts*, 2021, **11**, 400.
21 M. Zhu, Y. Dai, W. Fu, Y. Wu, X. Zou, T. You and Y. Sun, *Nanotechnology*, 2018, **29**, 165707.
22 Z. Shao, X. Cheng and Y. Zheng, *J. Colloid Interface Sci.*, 2018, **530**, 412–423.
23 Y. Chen, L. Yang, J. Chen and Y. Zheng, *J. Hazard. Mater.*, 2019, **371**, 576–585.
24 W. Fu, Y. Dai, J. Tian, C. Huang, Z. Liu, K. Liu, L. Yin, F. Huang, Y. Lu and Y. Sun, *Nanotechnology*, 2018, **29**, 345607.
25 X. Huang, C. Tian, H. Qin, W. Guo, P. Gao and H. Xiao, *Ceram. Int.*, 2020, **46**, 4679–4689.
26 W. Fu, Z. Li, W. Xu, Y. Wang, Y. Sun and Y. Dai, *Mater. Today Nano*, 2020, **11**, 100088.
27 J. Wu, O. Akampumuza, P. Liu, Z. Quan, H. Zhang, X. Qin, R. Wang and J. Yu, *Mater. Today Commun.*, 2020, **23**, 100897.
28 I. Chen and X. Wang, *Nature*, 2000, **404**, 168–171.
29 K. Liu, C. Liu, P. C. Hsu, J. Xu, B. Kong, T. Wu, R. Zhang, G. Zhou, W. Huang, J. Sun and Y. Cui, *ACS Cent. Sci.*, 2018, **4**, 894–898.
30 Y. Wang, W. Li, Y. Xia, X. Jiao and D. Chen, *J. Mater. Chem. A*, 2014, **2**, 15124–15131.
31 Z. Zhong, Z. Xu, T. Sheng, J. Yao, W. Xing and Y. Wang, *ACS Appl. Mater. Interfaces*, 2015, **7**, 21538–21544.
32 B. Tepekiran, M. Calisir, Y. Polat, Y. Akgul and A. Kilic, *Aerosol Sci. Technol.*, 2019, **53**, 921–932.
33 A. Yang, L. Cai, R. Zhang, J. Wang, P. Hsu, H. Wang, G. Zhou, J. Xu and Y. Cui, *Nano Lett.*, 2017, **17**, 3506–3510.
34 C. Wang, S. Wu, M. Jian, J. Xie, L. Xu, X. Yang, Q. Zheng and Y. Zhang, *Nano Res.*, 2016, **9**, 2590–2597.
35 S. Park, H. Koo, C. Yu and W. Choi, *Chem. Eng. J.*, 2021, **410**, 128302.
36 S. Pan, Y. Dong, Y. Zheng, L. Zhong and Z. Yuan, *J. Membr. Sci.*, 2017, **523**, 205.
37 R. Zhang, B. Liu, A. Yang, Y. Zhu, C. Liu, G. Zhou, J. Sun, P. Hsu, W. Zhao, D. Lin, Y. Liu, A. Pei, J. Xie, W. Chen, J. Xu, Y. Jin, T. Wu, X. Huang and Y. Cui, *Nano Lett.*, 2018, **18**, 1130–1138.
38 Y. Hunge, A. Yadav, S. Khan, K. Takagi, N. Suzuki, K. Teshima, C. Terashima and A. Fujishima, *J. Colloid Interface Sci.*, 2021, **582**, 1058–1066.
39 S. Dinoop, J. Sunil, C. Rajesh and K. Arun, *Polym. Degrad. Stab.*, 2021, **184**, 109476.
40 C. Dong, J. Ji, Z. Yang, Y. Xiao, M. Xing and J. Zhang, *Chin. Chem. Lett.*, 2019, **30**, 853–862.
41 D. Mateo, J. Cerrillo, S. Durini and J. Gascon, *Chem. Soc. Rev.*, 2021, **50**, 2173–2210.
42 J. Jetter, Z. Guo, J. McBrian and M. Flynn, *Sci. Total Environ.*, 2002, **295**, 51–67.
43 R. Sadri, M. Hosseini, S. Kazi, S. Bagheri, N. Zubir, K. Solangi, T. Zaharinie and A. Badarudin, *J. Colloid Interface Sci.*, 2017, **504**, 115–123.

44 C. Hu, X. Chen, J. Jin, Y. Han, S. Chen, H. Ju, J. Cai, Y. Qiu, C. Gao, C. Wang, Z. Qi, R. Long, L. Song, Z. Liu and Y. Xiong, *J. Am. Chem. Soc.*, 2019, **141**, 7807–7814.
45 J. Chen, J. Feng, Z. Li, P. Xu, X. Wang, W. Yin, M. Wang, X. Ge and Y. Yin, *Nano Lett.*, 2019, **19**, 400–407.
46 X. Li, H. Everitt and J. Liu, *Nano Res.*, 2020, **13**, 1268–1280.
47 Y. Wu, Y. Sun, W. Fu, X. Meng, M. Zhu, S. Ramakrishna and Y. Dai, *ACS Appl. Nano Mater.*, 2020, **3**, 2713–2722.
48 H. Wei, S. Loeb, N. Halas and J. Kim, *Proc. Natl. Acad. Sci. U. S. A.*, 2020, **117**, 15473–15481.
49 Y. Qin, M. Hao, C. Xu and Z. Li, *Green Chem.*, 2021, **23**, 4161–4169.
50 H. Li, F. Qin, Z. Yang, X. Cui, J. Wang and L. Zhang, *J. Am. Chem. Soc.*, 2017, **139**, 3513–3521.